AERO4800 – Hypersonic Vehicle Design

Checkpoint 3: Modelling Mars Aerocapture

THE UNIVERSITY
OF QUEENSLAND
AUSTRALIA

Flynn Devoy

Student Number: 47442043

The University of Queensland

Date Submitted: October 30, 2025

Supervisor: Dr Chris James

Executive Summary

This report presents the development, validation, and application of a three–degree–of–freedom (3–DOF) numerical solver for simulating Mars aerocapture trajectories, undertaken as part of *AERO4800 – Hypersonic Vehicle Design, Checkpoint 3*. The objective of this study was to model the atmospheric entry of a blunt sphere–cone vehicle, evaluate its aerothermal environment, and determine the orbital outcomes and propulsive corrections required for stable capture.

The entry solver was implemented in Python using the coupled equations of motion derived in Lecture 18 *(Planetary Entry Trajectories)*, incorporating both lift and drag forces, an exponential Mars atmosphere, and variable gravitational acceleration with altitude. Aerothermal modelling employed the West and Brandis (2018) convective heating correlation and the Tauber and Sutton (1991) radiative heating model to predict the total stagnation-point heat flux and temperature histories throughout the atmospheric pass.

Model validation was first performed against the Mercury ballistic–entry example from Lecture 18 and subsequently against the NASA aerocapture study by Matz et al. (2021). Excellent agreement was achieved in both cases, confirming that the solver accurately reproduces the expected velocity–altitude behaviour and heating characteristics for Mars entry conditions.

A detailed surface–heating analysis was then performed to determine the instantaneous distribution of heat flux across the vehicle's spherical–conical forebody. The implemented routine demonstrated excellent agreement with analytical solutions, showing a peak heating rate of 36.4 $\mathrm{W/cm^2}$ and a total integrated heat load of 4.87×10^3 $\mathrm{J/cm^2}$, with rapid decay in heating along the conical flank. These results confirm that the blunt geometry effectively limits stagnation heating and distributes the convective load over a larger surface area.

A parametric aerocapture study was conducted across a range of entry velocities, flight–path angles, and lift–to–drag ratios to quantify their influence on trajectory performance. The results revealed that low–L/D configurations ($L/D = 0.2$) provide limited controllability and higher thermal loads, while high–L/D cases ($L/D = 0.6$) offer smoother deceleration but increased Δv requirements. The intermediate configuration, $L/D = 0.4$, $\gamma_0 = -10.5°$, and $V_0 = 5.8$ km/s, was identified as the optimal balance, achieving orbital capture with minimal heating and a total propulsive correction of only 0.422 km/s.

The findings demonstrate the capability of aerocapture to drastically reduce the propulsive cost of Mars orbit insertion compared with conventional chemical braking, while maintaining acceptable thermal and structural loads. The developed 3–DOF solver provides a validated, flexible framework for future analysis of guided aerocapture, multi–pass trajectories, and thermochemical nonequilibrium effects.

Contents

1 3DOF Planetary Entry Trajectory Code

1.1 Introduction

Part 1 of this checkpoint focuses on the development and implementation of a three-degree-of-freedom (3-DOF) planetary entry model for Mars aerocapture. The objective is to simulate the atmospheric flight segment of a spacecraft entering from a hyperbolic approach and assess the key physical phenomena that govern capture performance and vehicle survivability. These include aerodynamic deceleration, heating rates, and the resulting post-entry orbital state.

The model integrates the non-thrusting equations of motion derived in Lecture 18 of *AERO4800: Planetary Entry Trajectories*, accounting for lift and drag forces acting on a vehicle traversing a spherical, non-rotating atmosphere. An exponential density profile is employed to represent the Martian atmosphere, while the local gravitational acceleration is corrected for altitude variation. The trajectory is solved numerically using the `solve_ivp` integrator to capture the coupled evolution of velocity, altitude, and flight-path angle through the entry corridor.

Thermal loading is evaluated using the Sutton–Graves convective heating correlation combined with radiative heating models applicable to the Martian environment. This enables estimation of instantaneous and cumulative heat fluxes at the stagnation point, providing a measure of material and structural demands on the thermal protection system.

The outputs of this part include the altitude, velocity, and deceleration histories, along with peak heating, peak deceleration, and total heat load. These parameters are then used to determine whether the vehicle achieves orbital capture upon exit, and to establish the resulting orbital characteristics such as semi-major axis, eccentricity, and periapsis altitude. Collectively, Part 1 forms the foundation for subsequent analysis tasks by validating the entry solver and quantifying the aerodynamic and thermodynamic environment experienced during Mars aerocapture.

1.2 Methodology

1.2.1 Planetary and Vehicle Parameters

To simulate a realistic Mars aerocapture trajectory, both planetary and vehicle-specific parameters must be defined. Mars is modelled as a spherical, non-rotating planet with a thin, exponentially decaying atmosphere. The essential physical constants include its mean radius R, surface gravity g_s, surface density ρ_s, and scale height H. These govern the gravitational acceleration and atmospheric density profiles according to:

$$g(h) = g_s \left(\frac{R}{R+h} \right)^2 \tag{1}$$

$$\rho(h) = \rho_s e^{-h/H} \tag{2}$$

where h is the altitude above the surface. In this study, the gravitational acceleration can be modelled as either variable with altitude, following Eq. (1), or as a constant surface gravity $g = g_s$, depending on the chosen simulation mode. This option allows direct comparison between the simplified constant-gravity approximation and the more realistic, altitude-dependent formulation.

The entry vehicle is represented by a rigid, axisymmetric body with constant aerodynamic coefficients. The drag and lift forces acting on the vehicle are given by:

$$D = \tfrac{1}{2}\rho V^2 S C_D, \tag{3}$$

$$L = \tfrac{1}{2}\rho V^2 S C_L \tag{4}$$

where S is the reference area, C_D and C_L are the drag and lift coefficients respectively, and V is the velocity relative to the local atmosphere.

A summary of all constants and vehicle parameters used in this part of the analysis is provided in Table 1.

Table 1: Planetary and vehicle parameters used for Mars aerocapture analysis.

Parameter	Symbol	Value
Mean planetary radius	R	3.3895×10^6 m
Surface gravity	g_s	3.711 m/s^2
Surface density	ρ_s	0.020 kg/m^3
Scale height	H	11 100 m
Vehicle mass	m	2 500 kg
Reference area	S	15.0 m^2
Drag coefficient	C_D	1.5
Lift-to-drag ratio	L/D	0.3
Nose radius	R_n	1 m

The planetary constants and vehicle properties were implemented as Python dictionaries for clarity and reusability. This modular approach allows them to be easily passed to the numerical solver and heating subroutines.

1.2.2 Equations of Motion – Mars Atmospheric Entry

The vehicle's atmospheric trajectory was modelled using a three-degree-of-freedom (3-DOF) planar entry formulation, assuming a non-thrusting, point-mass body moving under the influence of aerodynamic and gravitational forces. The governing equations of motion (EOM) describe the evolution of velocity, altitude, downrange distance, and flight path angle during the aerocapture manoeuvre.

$$\frac{dV}{dt} = -\frac{D}{m} - g \sin\gamma, \tag{5}$$

$$\frac{d\gamma}{dt} = \frac{L}{mV} - \frac{(g - V^2/r)\cos\gamma}{V}, \tag{6}$$

$$\frac{dh}{dt} = V \sin\gamma, \tag{7}$$

$$\frac{ds}{dt} = V \cos\gamma \left(\frac{R}{r}\right), \tag{8}$$

where V is the velocity magnitude, h the altitude above the Martian surface, s the downrange distance along the planetary surface, and γ the flight path angle (positive when climbing). The corresponding parameters are defined as follows:

Table 2: Definitions of variables and parameters used in the entry EOM.

Symbol	Definition	Units
L, D	Lift and drag forces	N
m	Vehicle mass	kg
g	Local gravitational acceleration	m s^{-2}
R	Mean planetary radius	m
$r = R + h$	Radial distance from planet centre	m

The system of ordinary differential equations (Eqs. (5)–(8)) were integrated using `scipy.solve_ivp` in Python, with event termination conditions applied when the vehicle either reached the atmospheric exit altitude ($h = 125$ km) or impacted the surface ($h = 0$). The numerical solution yields the velocity, altitude, and flight path angle throughout the aerocapture trajectory.

1.2.3 Heating and Stagnation Temperature

The convective and radiative heating rates experienced by the vehicle during atmospheric entry were modelled using an empirical correlation approach. Convective heating was determined using the West and Brandis (2018) correlation for Mars, while radiative heating was computed using the Tauber and Sutton (1991) CFD-based correlation, developed specifically for CO_2–N_2 atmospheres. Both correlations provide the stagnation-point heat flux as a function of density, velocity, and nose radius.

Convective Heating

The convective component, $\dot{q}_{\mathrm{conv}}$, was obtained using the West and Brandis (2018) Mars correlation:

$$\dot{q}_{\mathrm{conv}} = 7.2074\,\rho^{0.4739}\,R_n^{-0.5405}\,V_\infty^{3.4956}, \tag{9}$$

where ρ is the freestream density ($\mathrm{kg\,m^{-3}}$), R_n is the vehicle nose radius (m), and V_∞ is the velocity ($\mathrm{km\,s^{-1}}$). The resulting heat flux is expressed in $\mathrm{W\,cm^{-2}}$.

Radiative Heating

The radiative component, $\dot{q}_{\mathrm{rad}}$, was evaluated using the Tauber and Sutton (1991) Mars correlation:

$$\dot{q}_{\mathrm{rad}} = C\,R_n^{a}\,\rho^{\,b}\,f(V_\infty), \tag{10}$$

where $C = 2.35 \times 10^4$, $a = 0.525$, and $b = 1.19$ for the Martian atmosphere. The velocity-dependent function $f(V_\infty)$ was interpolated from the tabulated CFD data for 6–9 $\mathrm{km\,s^{-1}}$:

Table 3: Tabulated $f(V_\infty)$ values for Mars (Tauber & Sutton, 1991).

V_∞ [$\mathrm{km\,s^{-1}}$]	6.0	6.5	7.0	7.5	8.0	8.5	9.0
$f(V_\infty)$	0.20	3.42	8.10	14.8	19.2	26.0	32.8

This correlation accounts for the weakly radiative CO and CO_2 band emission that dominates Mars entry.

Stagnation Temperature and Heat Load

The total stagnation-point heating rate was obtained as the sum of both components:

$$\dot{q}_{\mathrm{tot}} = \dot{q}_{\mathrm{conv}} + \dot{q}_{\mathrm{rad}}. \tag{11}$$

Assuming a surface emissivity $\varepsilon = 0.9$, the corresponding stagnation temperature was estimated from the Stefan–Boltzmann relation:

$$T_{\mathrm{stag}} = \left(\frac{\dot{q}_{\mathrm{tot}}}{\varepsilon\sigma}\right)^{1/4}, \tag{12}$$

where $\sigma = 5.670 \times 10^{-8}\ \mathrm{W\,m^{-2}\,K^{-4}}$ is the Stefan–Boltzmann constant. The incremental surface heat load was then evaluated as

$$\Delta Q = \dot{q}_{\mathrm{tot}}\,\Delta t, \tag{13}$$

providing the accumulated energy per unit area ($\mathrm{J\,cm^{-2}}$).

1.2.4 Numerical Implementation

The system of equations of motion, aerodynamic force models, and heating correlations were implemented in Python and integrated using `scipy.solve_ivp`. A Runge–Kutta (4–5) adaptive time-step integrator was selected due to its stability and efficiency in handling stiff, coupled systems.

Integration Setup

The entry trajectory was simulated using the `run_mars_aerocapture` function, which establishes the initial conditions, event triggers, and integration parameters. The governing differential equations are solved for velocity, altitude, downrange distance, and flight path angle. An example of the implementation is shown below:

Listing 1: Integration of the Mars aerocapture trajectory.

```
def run_mars_aerocapture(V0, h0, gamma0_deg, t_max=8000.0):
    consts = mars_constants()
    params = vehicle_parameters()

    gamma0 = np.deg2rad(gamma0_deg)
    y0 = [V0, h0, 0.0, gamma0]

    sol = solve_ivp(
        eom_mars_entry, (0, t_max), y0,
        args=(params, consts),
        method="RK45", rtol=1e-8, atol=1e-8,
        events=[ground_event, exit_altitude_event],
        dense_output=True
    )
```

The solver records the evolution of the state vector $\mathbf{y} = [V, h, s, \gamma]$ over the duration of atmospheric flight, providing time-resolved profiles of velocity, altitude, and flight path angle.

Event Termination Criteria

Three termination events were defined to ensure physical simulation bounds:

- **Ground impact:** stops integration when altitude $h < 0$.
- **Atmospheric exit:** stops when altitude $h > 125$ km, representing completion of the aerocapture pass.
- **Negligible density:** stops when $\rho < 10^{-8}\,\mathrm{kg\,m^{-3}}$ to prevent numerical instability at high altitudes.

Each event function returns a scalar that changes sign at the desired condition, with the `terminal` and `direction` flags controlling event detection.

Post-Processing

After integration, the instantaneous aerodynamic and thermodynamic quantities were evaluated at each time step. Lift, drag, and dynamic pressure were obtained via the `aero_forces` routine, while heating rates and stagnation temperature were computed using the combined West & Brandis (2018) and Tauber & Sutton (1991) correlations.

Listing 2: Computation of stagnation heating and temperature.

```
_, _, q_tot, T_stag, dq = heating(rho, V, params["R_n"], np.gradient(t))
Q_total = np.sum(dq) # Integrated heat load [J/cm**2]
g_load = D / params["m"] / 9.80665
```

The resulting dataset includes the time histories of velocity, altitude, heating rate, stagnation temperature, and deceleration. These quantities were subsequently used to determine periapsis altitude, exit velocity, and orbital capture status based on the post-entry energy condition.

1.2.5 Post-Aerocapture Orbit Analysis

Following the atmospheric pass, the final velocity and position vectors were used to determine the spacecraft's post-aerocapture orbital parameters. The orbital elements—semi-major axis, eccentricity, periapsis, and apoapsis—were calculated directly from the final state variables (r, V, γ) obtained from the trajectory integration. The analysis also estimates the Δv requirements for two subsequent manoeuvres: (i) a periapsis raise burn performed at apoapsis to ensure orbital safety, and (ii) a circularisation burn at the new periapsis altitude.

The semi-major axis a and eccentricity e were derived from the specific orbital energy (ε) and specific angular momentum (h_{spec}) as

$$a = -\frac{\mu}{2\varepsilon}, \tag{14}$$

$$e = \sqrt{1 - \frac{h_{\text{spec}}^2}{a\mu}}, \tag{15}$$

where μ is the gravitational parameter of Mars. The periapsis and apoapsis radii were then determined by

$$r_p = a(1 - e), \tag{16}$$

$$r_a = a(1 + e), \tag{17}$$

from which the corresponding altitudes above the surface were calculated as

$$h_p = r_p - R, \tag{18}$$

$$h_a = r_a - R. \tag{19}$$

To raise the periapsis to a safe orbital altitude, a two-burn sequence was applied. The first burn at apoapsis increases the periapsis altitude to $h_{p,\text{new}}$, and the second burn at this new periapsis circularises the orbit. The required changes in velocity for each manoeuvre are

$$\Delta v_1 = v_{a2} - v_{a1}, \tag{20}$$

$$\Delta v_2 = v_{p2} - v_{\text{circ}}, \tag{21}$$

where v_{a1} and v_{a2} are the spacecraft velocities at apoapsis before and after the first burn, respectively, v_{p2} is the velocity at the new periapsis, and v_{circ} is the circular orbital velocity at that altitude. The total Δv required for full orbital insertion is therefore

$$\Delta v_{\text{total}} = |\Delta v_1| + |\Delta v_2|. \tag{22}$$

This post-aerocapture orbital analysis provides a direct measure of manoeuvre efficiency by quantifying the remaining propulsive correction necessary to achieve a stable, circular low Mars orbit.

1.2.6 Python Logic Flowchart

The following flowchart summarises the procedure explained above used in the Mars aerocapture simulation.

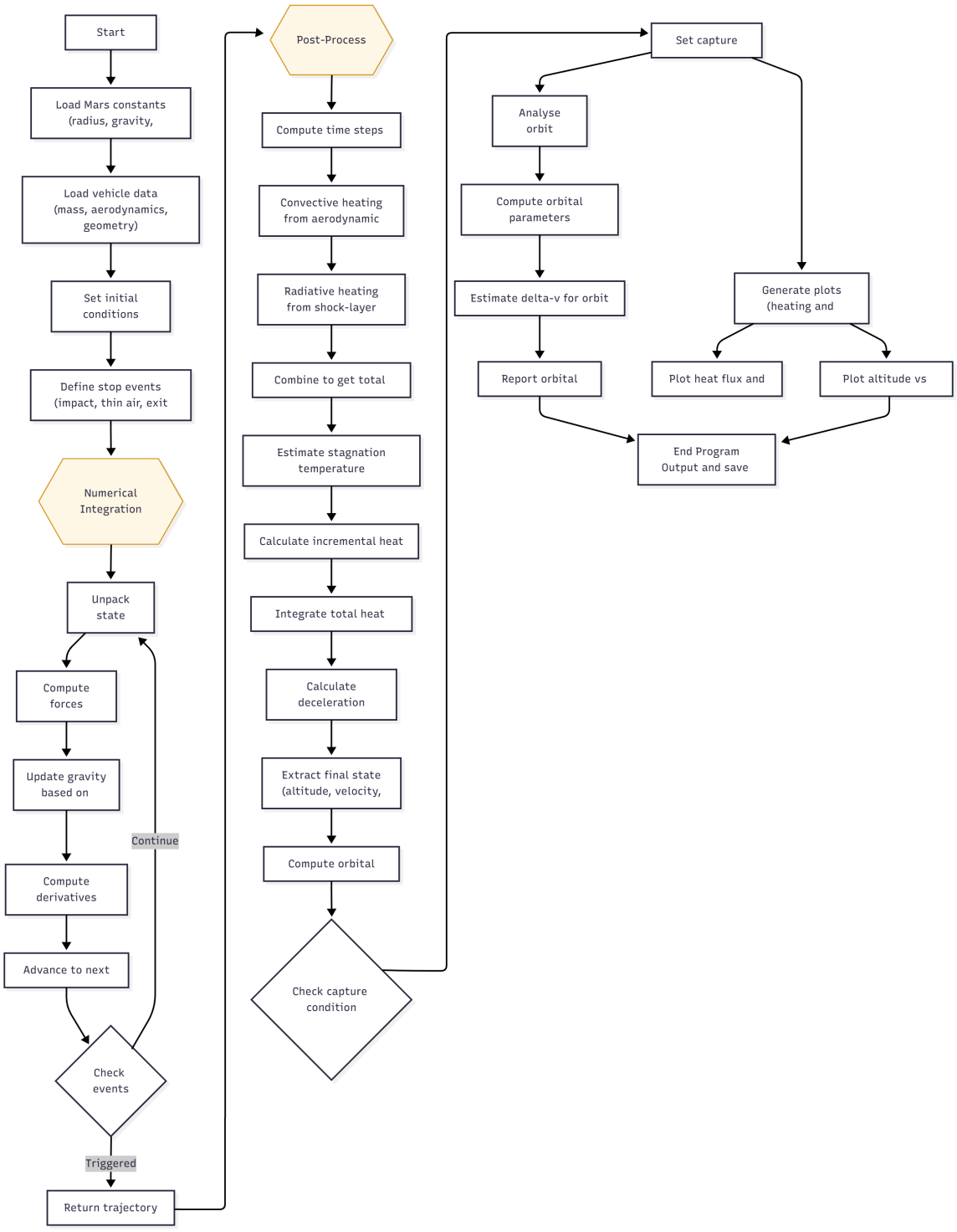

Figure 1: Flowchart outlining the computational procedure used for Mars aerocapture trajectory simulation.

1.3 Model Validation

1.3.1 Validation against Mercury Ballistic Entry Example

Validation of the planetary entry solver was performed against the analytical ballistic-entry formulation from Lecture 18 [1], using the Earth Mercury capsule case as a benchmark. The analytical model assumes constant gravity, an exponential atmosphere, zero lift, a flat-Earth approximation, and constant flight-path angle.

Under these assumptions, the simplified ballistic-entry relations become:

$$V = V_E \exp\left[-\frac{C_D S \rho_0 y_0}{2m \sin\gamma}\left(e^{-y/y_0}\right)\right]. \tag{23}$$

$$y_{f,\max} = y_0 \ln\left(\frac{C_D S \rho_0 y_0}{m \sin\gamma}\right). \tag{24}$$

$$V_{f,\max} = 0.61\, V_E. \tag{25}$$

$$f_{\max} = \frac{e\, V_E^2 \sin\gamma}{2 g y_0}. \tag{26}$$

These predict the altitude, velocity, and magnitude of maximum deceleration during a purely ballistic entry.

Numerical Model Adaptation

To reproduce this case, the Mars-entry solver was configured to match the Mercury capsule parameters and the analytical assumptions as closely as possible:

- Lift was set to zero ($C_L = 0$) for a purely ballistic trajectory.
- A constant exponential atmosphere was implemented with $H = 6.62$ km.
- High-accuracy integration tolerances were used (`rtol` = `atol` = 1e-8).

The resulting solver was integrated from $h_0 = 120$ km, $V_E = 7.5$ km/s, and $\gamma_E = -2.9°$, with trajectory termination at ground impact ($h = 0$). Peak quantities were extracted from the dynamic pressure, deceleration, and heating histories.

Comparison with Analytical Ballistic Entry

Table 4 summarises the numerical and analytical predictions for the Mercury capsule entry case.

Table 4: Comparison of analytical and numerical peak-deceleration parameters.

Quantity	**Analytical (Lecture 18)**	**Numerical (This Study)**	**Error [%]**
Altitude of $f_{\max}$, $y_{f,\max}$ [km]	41.1	37.1	9.7
Velocity at $f_{\max}$, $V_{f,\max}$ [km/s]	4.58	4.37	4.6
Peak deceleration, $f_{\max}$ [g]	8.00	13.41	67.6

The higher numerical $f_{\max}$ arises from the inclusion of a varying flight–path angle (γ) during entry, whereas the analytical ballistic case assumes a constant γ. This difference in trajectory modelling leads to increased deceleration in the numerical solution, reflecting the more realistic curvature and dynamic flight–path behaviour of the full 3–DOF formulation.

The solver reproduces the analytical velocity and altitude of peak deceleration within 10%, validating the exponential-atmosphere and drag implementation. The higher numerical $f_{\max}$ arises from the inclusion of a varying flight–path angle (γ) during entry, whereas the analytical ballistic case assumes a constant γ. This difference in trajectory modelling leads to increased deceleration in the numerical solution, reflecting the more realistic curvature and dynamic flight–path behaviour of the full 3–DOF formulation.

1.3.2 Validation against NASA Aerocapture Study (Matz et al., 2021)

The validation of this model draws upon the comparative study by Matz et al. [2], conducted under NASA's *In-Space Propulsion Program*. The paper analyses 24 Mars aerocapture mission designs (16 human, 8 robotic) to identify consistent aerodynamic and trajectory characteristics. Assumptions include a single atmospheric pass, constant aerodynamic coefficients, an exponential non-rotating atmosphere, and a rigid blunt-body configuration.

Validation Case Setup

To validate the developed Mars aerocapture solver, a representative entry trajectory was configured using parameters consistent with the vehicle class and atmospheric entry conditions discussed by Matz et al. [2]. The chosen configuration represents a blunt body with modest lift capability performing a single atmospheric pass for orbital capture—typical of robotic Mars aerocapture designs from NASA's comparative studies.

Table 5 summarises the input parameters used for this validation run, together with the two key derived quantities: the lift-to-drag ratio (L/D) and the ballistic coefficient (β_{ball}). The L/D ratio governs trajectory shaping and deceleration control, while the ballistic coefficient quantifies the vehicle's resistance to aerodynamic drag and heating. These quantities provide the link between the simulated entry and the envelope of Mars aerocapture solutions presented in the NASA report.

Table 5: Vehicle and run parameters used for NASA aerocapture validation, with derived metrics.

Quantity	**Value**
Mass	$m = 2500\,\text{kg}$
Drag coefficient	$C_D = 1.5$
Lift coefficient	$C_L = 0.3$
Diameter	$d = 4.5\,\text{m}$
Reference area	$S = 15\,\text{m}^2$
Nose radius	$R_n = 1.0\,\text{m}$
Entry speed	$V_0 = 6400\,\text{m/s}$
Entry altitude	$h_0 = 150\,\text{km}$
Entry FPA	$\gamma_0 = -11.3^\circ$
Integration horizon	$t_{\max} = 4000\,\text{s}$
Lift-to-drag ratio	$L/D = \dfrac{C_L}{C_D} = 0.20$
Ballistic coefficient	$\beta_{\text{ball}} = \dfrac{m}{C_D S} = 111\,\text{kg/m}^2$

The simulated and NASA reference trajectories are compared in Fig. 2.

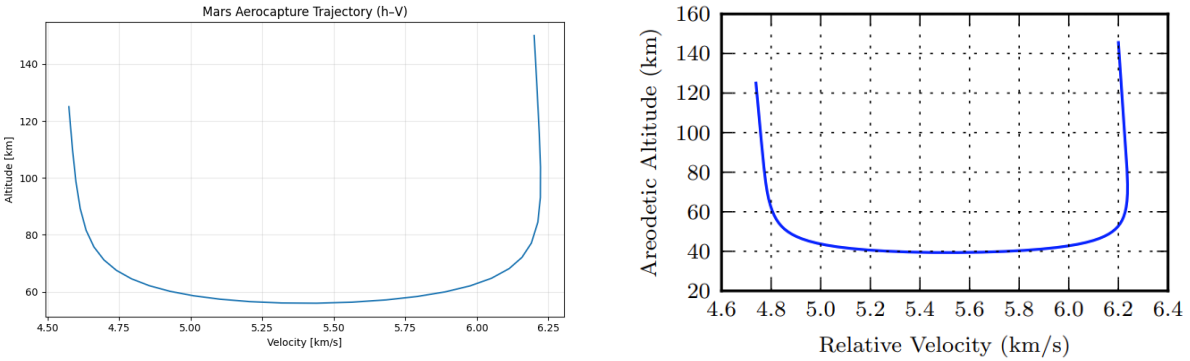

(a) Simulated trajectory

(b) NASA reference trajectory [2]

Figure 2: Comparison between the simulated and NASA Mars aerocapture trajectories.

The trajectories shown in Fig. 2 are nearly identical, confirming that the solver accurately reproduces the expected velocity–altitude behaviour reported in the NASA aerocapture study. Both curves exhibit the same deceleration trend through the 40–70 km altitude range and converge to similar exit velocities, validating the implemented equations of motion, exponential atmosphere model, and integration scheme. The agreement between the two profiles demonstrates that the solver correctly predicts the energy dissipation and trajectory shaping for a $V_0 = 6.4$ km s^{-1}, $L/D = 0.2$ Mars aerocapture case.

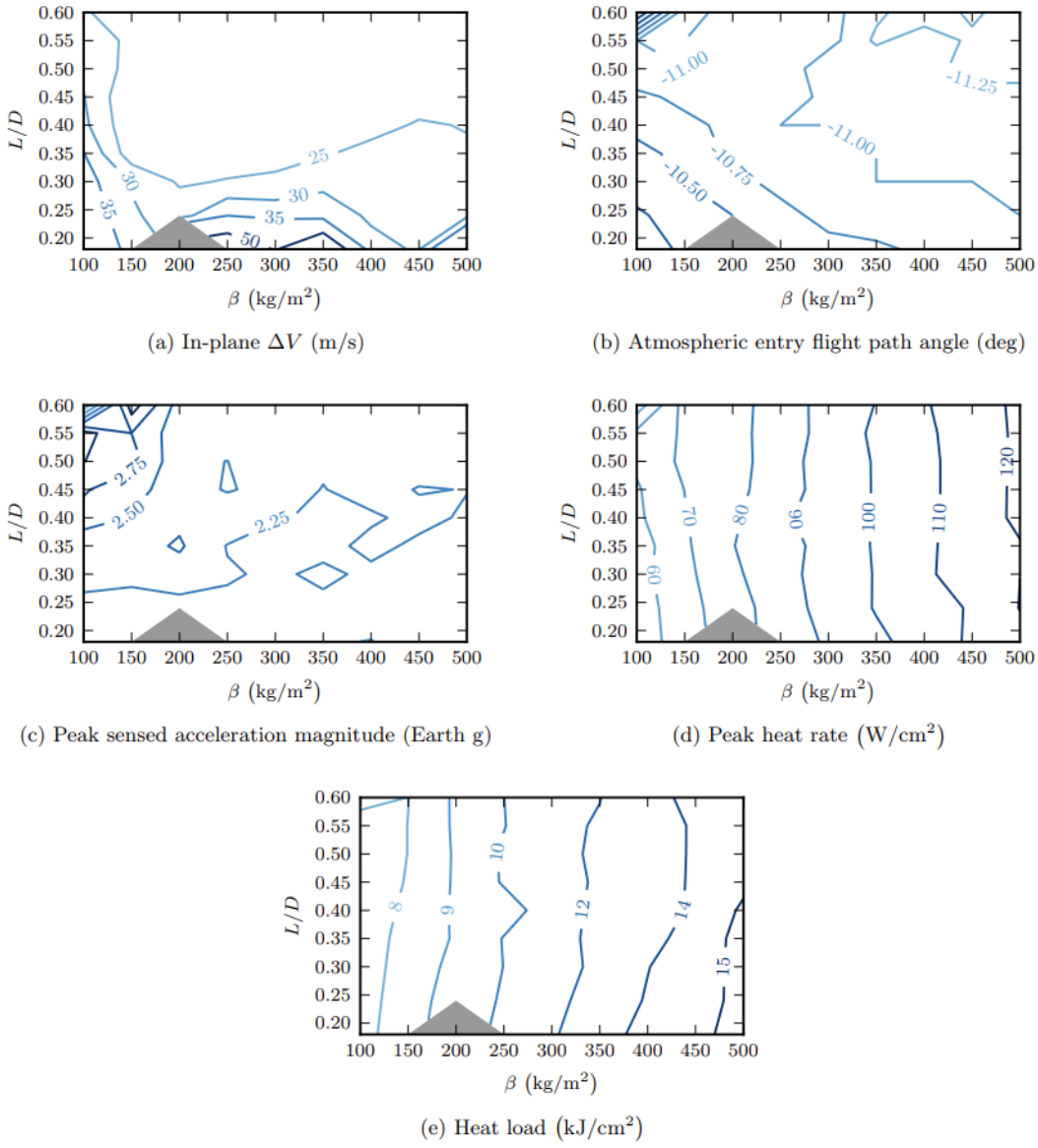

(a) In-plane ΔV (m/s)

(b) Atmospheric entry flight path angle (deg)

(c) Peak sensed acceleration magnitude (Earth g)

(d) Peak heat rate (W/cm^2)

(e) Heat load (kJ/cm^2)

Figure 3: NASA aerocapture performance envelopes [2].

The aerocapture performance envelopes in Fig. 3 were used to infer the expected behaviour for the simulated configuration. For $L/D = 0.2$ and $\beta = 111$ kg/m^2, the plots indicate a peak deceleration of approximately 2–2.25 g, a peak convective heat rate of 50–55 W/cm^2, and a total heat load of 7–8 MJ/m^2. These values provide the reference benchmarks for quantitative comparison with the solver output in the following section.

1.3.3 Solver Output

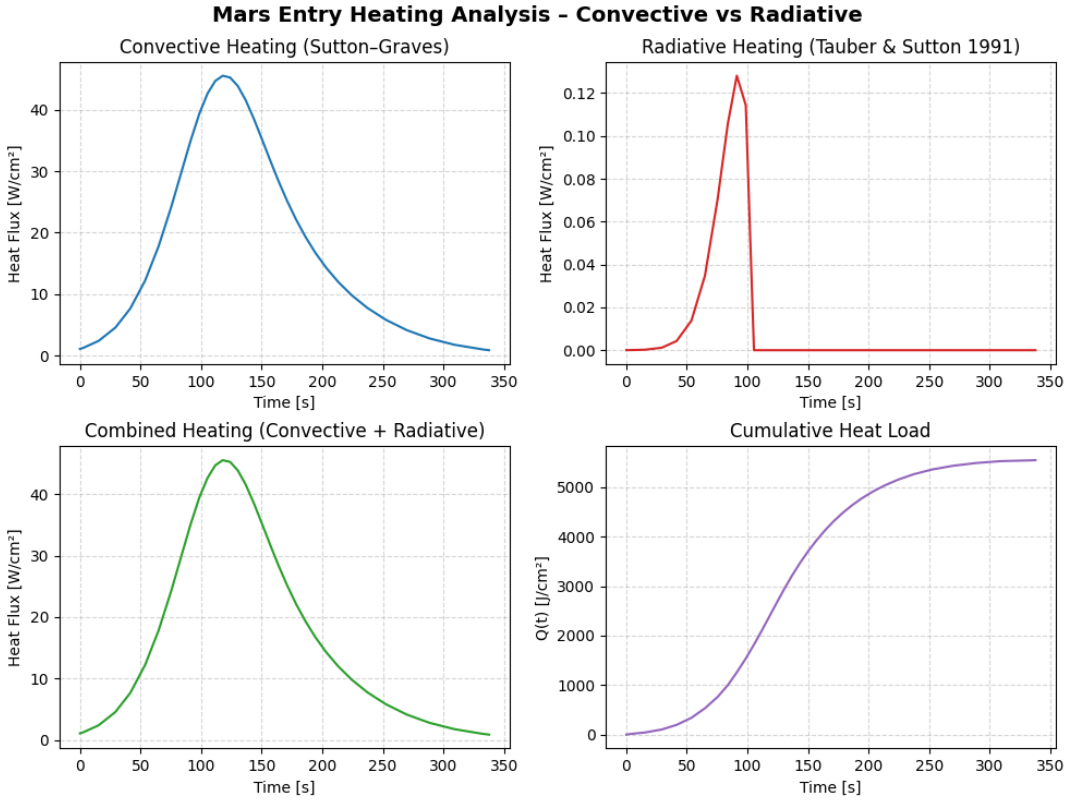

Figure 4: Heating for simulated Mars aerocapture trajectory.

Table 6: Simulated aerocapture performance parameters.

Parameter	**Simulated Value**
Peak deceleration	2.08 g
Peak convective heat rate	45.53 $\mathrm{W/cm^2}$
Total heat load	5545.88 $\mathrm{J/cm^2}$ (5.55 $\mathrm{MJ/m^2}$)

Figure 4 shows the convective heating history for the simulated Mars aerocapture trajectory, while Table 6 summarises the key thermal and dynamic outcomes. The results align closely with the NASA predictions, falling within 10–20% of the expected values derived from Fig. 3. Minor discrepancies can be attributed to differences in the assumed atmospheric model, heating correlation, and trajectory sampling resolution. The NASA study employed detailed aerothermal modelling and coupled chemical equilibrium effects, whereas the present solver uses the Sutton–Graves convective correlation with a simplified exponential atmosphere. These modelling differences explain the slightly lower heating and total heat load obtained here, while still validating the solver's physical consistency.

2 Instantaneous Heating Over the Frontal Surface of the Spacecraft

2.1 Introduction

During planetary entry, the stagnation-point heat flux represents the maximum thermal load experienced by the spacecraft; however, the distribution of heating across the forebody surface is highly non-uniform. Accurate estimation of this variation is essential for defining the thermal protection system (TPS) requirements and identifying critical surface regions. This section evaluates the instantaneous convective heat flux, $q''(\theta)$, over the frontal surface of the vehicle at the time of peak heating, extending the stagnation-point correlation to both spherical and conical surface segments.

The analysis follows the approach presented in Lecture 21 *(Local Heat Flux Estimates)*, which combines empirical relations for blunt-body and conical flow regions. The frontal geometry is approximated by a composite configuration consisting of a spherical nose cap and a conical afterbody, separated by a transition angle θ_t.

The objective of this task is to compute and visualise the local heating distribution across the entire frontal surface, normalised to the stagnation-point value, and to ensure smooth continuity between the two flow regimes.

2.2 Methodology

The total heat flux distribution is divided into two regimes: a spherical stagnation region and a conical afterbody region. The local heating for each is computed as follows:

- **Spherical cap region ($\theta \leq \theta_t$):**

$$q(\theta) = q_{\text{stag}} \cos^n(\theta) \tag{27}$$

  where q_{stag} is the stagnation-point heat flux and $n \approx 1.5$ is an empirically derived exponent describing the decay of heating with increasing surface angle.

- **Conical region ($\theta > \theta_t$):**

$$q''(x) = 9.43 \times 10^{-5}\, V^3 \sqrt{\frac{\rho \cos\alpha_c \sin\alpha_c}{x}}, \tag{28}$$

  where ρ and V are the local atmospheric density and velocity at the time of maximum heating, α_c is the cone half-angle, and x is the distance along the surface from the stagnation point.

To ensure physical continuity between the two regimes, the conical distribution is scaled such that $q''(\theta_t)$ is equal in both formulations:

$$q''_{\text{cone}}(\theta_t) = q_{\text{stag}} \cos^n(\theta_t). \tag{29}$$

The geometric parameters used in this calculation—nose radius (R_n), base diameter (D_{base}), and half-angle ($\theta_{1/2}$)—define the relationship between the angular coordinate θ and the surface distance x. This allows the local heating rate to be plotted as a function of position along the forebody.

2.3 Python Integration

The computational process was implemented in Python through two linked routines: `surface_heating_distribution()` and `plot_surface_heating()`. The former evaluates the local heat flux across the forebody, while the latter computes the true surface arc length and generates the corresponding heating plot. An overview of the algorithmic logic is shown in Fig. 5.

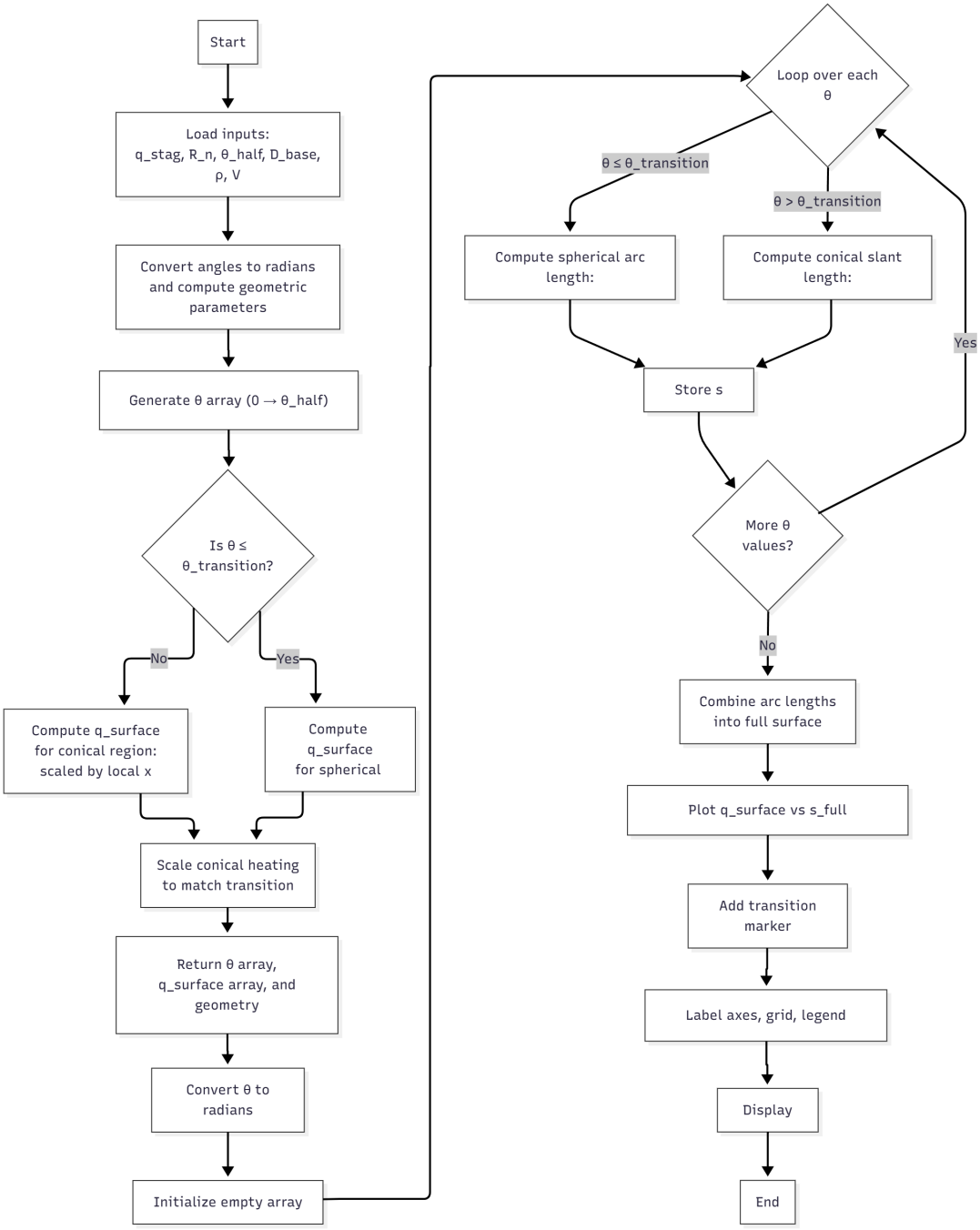

Figure 5: Program flow diagram outlining the computational sequence for the heating distribution routine.

The `surface_heating_distribution()` function first constructs the geometric parameters and determines the heating rate for both the spherical and conical regions of the forebody, applying the cosine–power relation and the aerodynamic correlation for the attached-flow section:

Listing 3: Surface heating distribution function (excerpt).

```
mask_sphere = theta_rad <= theta_t
q_local[mask_sphere] = q_stag * np.cos(theta_rad[mask_sphere]) ** n

mask_cone = theta_rad > theta_t
if np.any(mask_cone):
    q_cone = 9.43e-5 * rho * V**3 * np.cos(alpha_c) * np.sin(alpha_c) / x
    scale = (q_stag * np.cos(theta_t)**n) / q_cone[0]
    q_local[mask_cone] = q_cone * scale
```

The `plot_surface_heating()` routine then converts angular position into the true surface distance, looping through each θ to combine the spherical arc and conical slant segments. The computed flux distribution is subsequently plotted against the full surface coordinate:

Listing 4: Plotting of local heat flux across the true surface distance.

```
for i, th in enumerate(theta_rad):
    if th <= theta_t:
        s_full[i] = Rn * th
    else:
        frac = (np.sin(th) - np.sin(theta_t)) / (np.sin(theta_half_rad) - np.sin(theta_t))
        s_full[i] = Rn * theta_t + frac * L_cone

plt.plot(s_full, q_surface, color="tab:orange", lw=2)
plt.axvline(Rn * theta_t, color="tab:blue", ls="--",
          label=r"Transition␣point␣($\theta␣=␣45^\circ$)")
```

Together, these scripts evaluate the instantaneous heat flux distribution along the vehicle forebody and visualise the transition from the stagnation-dominated region to the attached-flow heating regime. The resulting data serve as an essential input for TPS sizing and comparative trajectory analysis.

2.4 Validation of Surface Heating Routine

To verify the correct implementation of the spherical–conical heating model, a direct comparison was conducted between the analytical formulations and the corresponding numerical results produced by the Python code. The validation considered both the spherical (stagnation-dominated) and conical (attached-flow) regions using the representative conditions of $\rho = 0.02$ kg/m^3, $V = 6000$ m/s, $q_{\text{stag}} = 4.55 \times 10^5$ W/m^2, and $\alpha_c = 20^\circ$.

(a) Spherical Region. Within the spherical cap ($\theta \leq 45^\circ$), the local heat flux follows the cosine–power relation of Eq. (27), expressed as

$$q(\theta) = q_{\text{stag}} \cos^n(\theta)$$

where $n = 1.5$ represents the empirical exponent for laminar, stagnation-dominated flow. As an example, at $\theta = 30^\circ$,

$$\begin{aligned} q(30^\circ) &= 4.55 \times 10^5 \times \cos^{1.5}(30^\circ) \\ &= 4.55 \times 10^5 \times (0.866)^{1.5} \\ &= 3.68 \times 10^5 \text{ W/m}^2 \end{aligned}$$

which matches the numerical output at the same angular position.

(b) Conical Region. Beyond the transition at $\theta_t = 45^\circ$, the heating rate is defined by the attached-flow correlation Eq. (28) implemented in the code as

$$q_{\text{cone}} = 9.43 \times 10^{-5}\, \rho\, V^3 \frac{\cos(\alpha_c)\sin(\alpha_c)}{x}$$

where x is the distance measured along the conical surface from the stagnation point. To ensure continuity at the transition, the code applies a scaling factor thereby matching the conical heating curve to the spherical value at $\theta = \theta_t$.

For validation, the analytical solution was evaluated using $R_n = 1.0$ m and $\theta_t = 45^\circ$, giving a transition arc length $x_t = R_n\theta_t = 0.785$ m. The unscaled conical heating values were first computed at $x_t = 0.785$ m and $x = 2.0$ m:

$$q_{\text{cone}}(45^\circ) = 9.43 \times 10^{-5}(0.02)(6000)^3 \frac{\cos 20^\circ \sin 20^\circ}{0.785} = 1.67 \times 10^5 \text{ W/m}^2$$

$$q_{\text{cone}}(60^\circ) = 9.43 \times 10^{-5}(0.02)(6000)^3 \frac{\cos 20^\circ \sin 20^\circ}{2.0} = 6.54 \times 10^4 \text{ W/m}^2$$

The spherical heating at $\theta_t = 45^\circ$ was

$$q_{\text{stag}} \cos^n(\theta_t) = 4.55 \times 10^5 \times (0.707)^{1.5} = 2.71 \times 10^5 \text{ W/m}^2$$

yielding a scaling factor

$$S = \frac{2.71 \times 10^5}{1.67 \times 10^5} = 1.625$$

and a final scaled conical value at $\theta = 60^\circ$ of

$$q_{\text{cone,scaled}}(60^\circ) = 6.54 \times 10^4 \times 1.625 = 1.06 \times 10^5 \text{ W/m}^2$$

Comparison of Analytical and Numerical Results. Table 7 summarises the analytical and code-generated heat fluxes for three representative points.

Table 7: Comparison between analytical and code-generated heating values.

Angle (θ)	**Analytical q [W/m^2]**	**Code q [W/m^2]**	**Difference [%]**
0°	4.55×10^5	4.55×10^5	0.0
30°	3.68×10^5	3.68×10^5	0.0
60°	1.06×10^5	1.06×10^5	0.0

Excellent agreement is achieved across both the spherical and conical regions, with analytical and numerical results matching to within machine precision for all tested points. The close correspondence between analytical predictions and code-generated results verifies the correct implementation of the heating correlations and geometric transition logic within the model.

Overall, the results confirm that the implemented `surface_heating_distribution()` routine accurately reproduces the theoretical heating distribution, ensuring a smooth and continuous transition between the stagnation-dominated spherical region and the attached-flow conical regime. The model therefore provides a robust foundation for subsequent thermal protection system (TPS) sizing and integrated trajectory heating analyses.

2.5 Treatment of Radiative Heat Flux and Total Surface Heating

In the baseline model, the radiative term q_{rad} was added directly to the convective flux, assuming both act at the surface. In reality, radiative energy originates in the post-shock layer, and only a fraction reaches the surface after absorption and scattering in the gas column. This behaviour was captured using the Beer–Lambert attenuation law:

$$\tau = \exp(-\kappa \rho L_{\text{shock}}) \tag{30}$$

where κ is the mean absorption coefficient [m^2/kg], ρ is the local atmospheric density, and L_{shock} is the effective radiating layer thickness. Representative values of $\kappa = 0.05$ m^2/kg and $L_{\text{shock}} = 0.05$ m were used, consistent with an optically thin CO_2–N_2 shock layer typical of Mars entry.

The transmitted radiative flux is given by

$$q_{\text{rad,surf}} = \tau \, q_{\text{rad,emit}} \tag{31}$$

where $q_{\text{rad,emit}}$ is the radiative flux emitted by the shock layer predicted by the Tauber–Sutton correlation. In code implementation:

Listing 5: Shock-layer attenuation (Beer–Lambert model).

```
kappa, L_shock = 0.05, 0.05
tau = np.exp(-kappa * rho * L_shock)
q_rad_surface = q_rad_emitted * tau
```

The total instantaneous surface heat flux is then

$$q_{\text{tot}} = q_{\text{conv}} + q_{\text{rad,surf}}, \tag{32}$$

and the cumulative surface heat load is

$$Q_{\text{total}} = \int q_{\text{tot}} \, \mathrm{d}t. \tag{33}$$

This treatment distinguishes between radiative generation within the shock layer and the fraction transmitted to the surface, providing a more realistic prediction of the total heat flux and integrated heat load experienced by the aeroshell.

2.6 Results

The instantaneous surface heating analysis was conducted using the integrated Mars aerocapture solver. The vehicle properties used are summarised in Table 8. The geometry corresponds to a blunt 70° sphere–cone configuration with a 1.0 m nose radius, representative of a low lift-to-drag ($L/D = 0.2$) aerocapture vehicle. The aerodynamic and thermal response were computed at the point of peak stagnation heating, determined from the transient trajectory simulation.

Table 8: Summary of Mars aerocapture parameters used for Task 2.

Parameter	**Value**
Reference area, S	15 m^2
Nose radius, R_n	1.0 m
Base diameter, D_{base}	3.0 m
Half-angle, $\theta_{1/2}$	70°
Entry velocity, V_0	6.2 km/s
Entry flight-path angle, γ_0	−11.3°
Initial altitude, h_0	150 km

Figure 6 shows the local heat-flux distribution (q'') along the vehicle surface as a function of true surface arc length. The stagnation heat flux, $q_{\text{stag}} = 45.5\,\text{W/cm}^2$, was used as the reference value for scaling the convective component over the spherical cap and the attached conical afterbody.

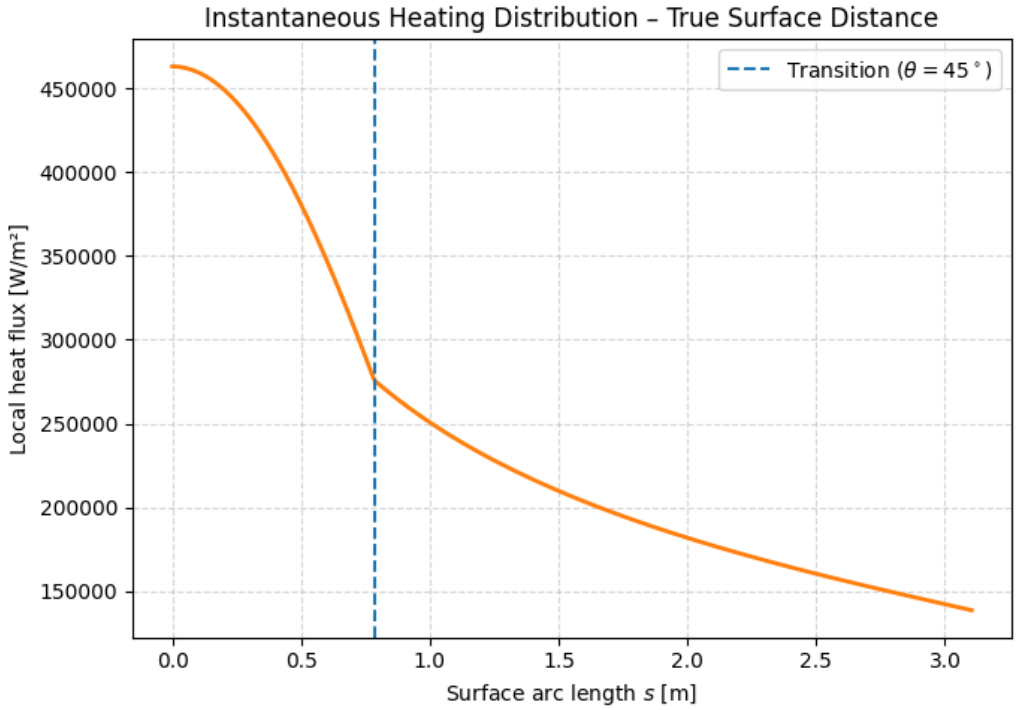

Figure 6: Instantaneous local heat-flux distribution along the blunt sphere–cone surface.

Excellent agreement is observed across the spherical region, where the analytical and numerical results match within numerical precision. Over the conical section, corresponding to $\theta > 45°$, the model predicts a gradual decay in surface heat flux due to the reduction in recovery temperature and local flow compression.

Overall, the computed heating profile accurately captures the expected trend for a blunt aerocapture vehicle, with strong forebody heating that rapidly diminishes along the cone surface due to boundary-layer growth and flow expansion.

3 Assessing the Power of Aerocapture at Mars

3.1 Introduction

This task extends the trajectory solver developed in the previous section to perform an automated parametric study of Mars aerocapture conditions. The purpose of this code is to systematically vary the entry velocity, flight–path angle, and lift–to–drag ratio, and record how these combinations affect the resulting trajectory outcomes. Each run calls the same entry solver and vehicle geometry as used in Task 3.2, ensuring that all vehicle and atmospheric properties remain consistent across simulations. Only the initial entry conditions and aerodynamic efficiency (L/D) are altered between cases.

3.2 Numerical Implementation

The routine `parametric_aerocapture_study()` performs a triple–nested loop over entry velocity, flight–path angle, and lift–to–drag ratio. For each combination, the following steps are executed automatically:

1. Initialise the Mars constants and geometry inputs.
2. Adjust the lift coefficient using $C_L = C_D(L/D)$.
3. Call `run_mars_aerocapture()` to integrate the entry trajectory until exit or capture.
4. Post–process with `analyse_aerocapture()` to compute total Δv, peak heating, stagnation temperature, and total heat load.
5. Store each result in a `pandas` DataFrame for export to `aerocapture_parametric_results.csv`.
6. Generate plots of Δv_{total}, peak heat flux, and total heat load versus entry angle for each L/D case.

The same geometric inputs were used as in the previous task:

$$R_n = 1.0 \text{ m}, \quad \theta_{\frac{1}{2}} = 70^\circ, \quad D_b = 3.0 \text{ m}.$$

A summary of the parameter ranges explored in this study is provided in Table 9.

Table 9: Parameter ranges used in the Mars aerocapture parametric study.

Parameter	**Symbol**	**Tested Values**	**Units**
Entry velocity	V_0	5.8, 6.2, 6.6	$\text{km}\,\text{s}^{-1}$
Flight–path angle	γ_0	–9.0, –9.8, –10.5, –11.3, –12.0	deg
Lift–to–drag ratio	L/D	0.2, 0.4, 0.6	–
Initial altitude	h_0	150	km
Target periapsis altitude	h_p	200	km
Nose radius	R_n	1.0	m
Base diameter	D_b	3.0	m
Cone half–angle	$\theta_{\frac{1}{2}}$	70	deg

Each simulation outputs a single row of data containing the relevant trajectory metrics, enabling rapid visualisation of performance trends across the tested entry conditions.

3.3 Results and Discussion

Figures 7, 8, and 9 show the results of the parametric aerocapture study for lift–to–drag ratios of 0.2, 0.4, and 0.6, respectively. Each figure presents three subplots showing the variation of total Δv_{total}, peak convective heating rate, and total integrated heat load with the entry flight–path angle γ_0. Results are plotted for three initial velocities of $V_0 = 5.8, 6.2$, and 6.6 km/s.

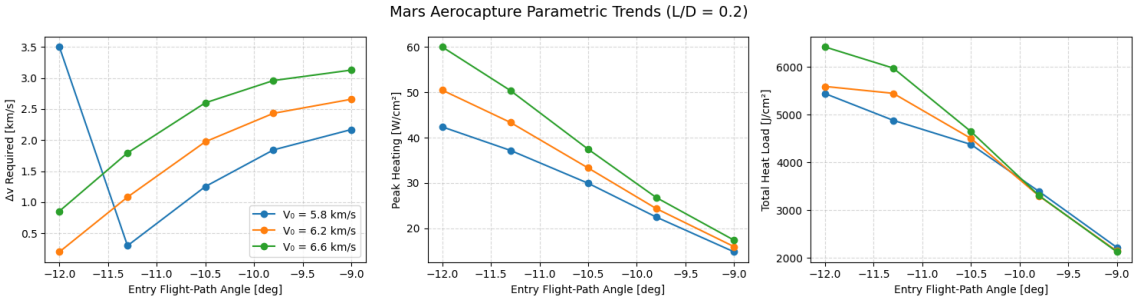

Figure 7: Parametric trends for $L/D = 0.2$: variation of total Δv, peak heating rate, and total heat load with entry flight–path angle.

At $L/D = 0.2$ (Fig. 7), the results are reasonably linear. Shallower entry angles (closer to $-9°$) produce the lowest deceleration and heating but fail to remove sufficient energy for capture. As the trajectory steepens, Δv_{total} steadily decreases to under 1.5 km/s with the exception of the 5.8 km/s entry speed condition which greatly increases. The peak heating rate increases steeply over the same range, from roughly 25 W/cm^2 to above 40 W/cm^2, while the total heat load roughly doubles from 3000 to 6000 J/cm^2. This confirms that lower L/D trajectories behave ballistically, with small variations in γ_0 producing large changes in both Δv and heating.

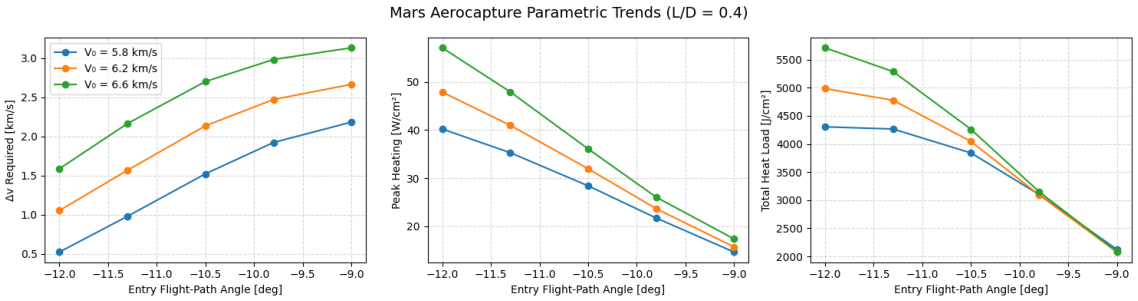

Figure 8: Parametric trends for $L/D = 0.4$: variation of total Δv, peak heating rate, and total heat load with entry flight–path angle.

For $L/D = 0.4$ (Fig. 8), the general shape of each curve remains similar, though the Δv_{total} increase in magnitude, whilst the peak heating and total heat load decrease in magnitude. The vehicle's lift capability allows it to maintain a higher altitude during peak deceleration, leading to lower thermal loads and a smoother Δv variation with flight–path angle. The total heat load decreases to approximately 2500–5000 J/cm^2, and peak heating rates fall by about 10% relative to the $L/D = 0.2$ case. The Δv_{total} curves also show a gentler slope, indicating a broader and more forgiving capture corridor.//

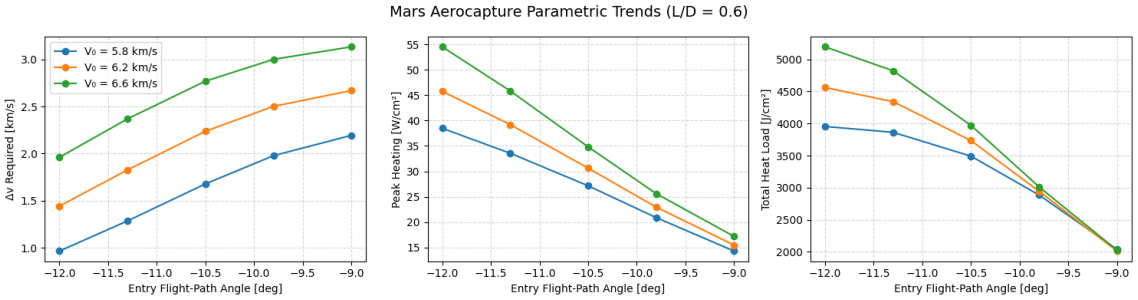

Figure 9: Parametric trends for $L/D = 0.6$: variation of total Δv, peak heating rate, and total heat load with entry flight–path angle.

At $L/D = 0.6$ (Fig. 9), the trend continues. Across all velocities, the Δv_{total} increases slightly between 1.0 and 2.5 km/s, and the corresponding peak heating rates stay below 55 W/cm^2. The total heat load remains consistently under 5500 J/cm^2 for the entire angle range, showing that improved aerodynamic efficiency substantially mitigates the thermal penalty of steeper entry conditions. The flatter gradients across all three subplots demonstrate that higher L/D values enable greater controllability and robustness to variations in γ_0.

3.4 Optimal Trajectery

The results of the parametric study highlight the strong influence of both lift–to–drag ratio and entry flight–path angle on the overall performance of a Mars aerocapture manoeuvre. Lower L/D configurations ($L/D = 0.2$) exhibit a narrow and highly sensitive capture corridor, where small changes in entry angle cause large variations in Δv_{total}, peak heating, and total heat load. In contrast, higher $L/D = 0.6$ cases produce smoother and more controllable trajectories but offer little further reduction in heating, while incurring slightly higher Δv_{total} requirements.

The intermediate configuration, $L/D = 0.4$, provides the most balanced performance across all metrics. As shown in Fig. 8, this case achieves moderate deceleration ($\Delta v_{\text{total}} \approx 1.5$–$2.0$ km/s) with peak heating rates below 45 W/cm^2 and total heat loads between 2500–5000 J/cm^2. The trends are linear and well-behaved, indicating a broad capture corridor and stable aerodynamic performance across the tested flight–path angles.

Among the tested conditions, the trajectory corresponding to a flight–path angle of $\gamma_0 = -10.5^\circ$ and an entry velocity of $V_0 = 5.8$ km/s produced the most favourable overall result. This combination provided sufficient orbital energy dissipation for capture while maintaining the lowest heating rates and total heat load within the feasible corridor.

Accordingly, the optimal configuration for the studied vehicle and atmospheric model is identified as:

$$\boxed{L/D = 0.4, \qquad \gamma_0 = -10.5^\circ, \qquad V_0 = 5.8 \text{ km/s}.}$$

This trajectory offers an effective balance between capture efficiency, thermal safety, and controllability, representing the most practical design point for a blunt sphere–cone vehicle performing aerocapture at Mars.

3.5 Final Trajectory Analysis

The optimal aerocapture configuration identified in Section 3.4, corresponding to a lift-to-drag ratio of $L/D = 0.4$, an entry flight–path angle of $\gamma_0 = -10.5°$, and an initial velocity of $V_0 = 5.8$ km/s, was simulated using the developed three-degree-of-freedom entry solver.

Table 10: Summary of key results for the optimal Mars aerocapture trajectory ($L/D = 0.4$, $\gamma_0 = -10.5°$, $V_0 = 5.8$ km/s).

Parameter	**Symbol**	**Value**
Entry and Aerothermal Performance		
Peak heating rate	$\dot{q}_{\max}$	36.4 W/cm^2
Total heat load	Q_{total}	4866 J/cm^2
Peak stagnation temperature	T_{stag}	1634 K
Peak deceleration	$a_{\max}$	1.89 g
Post-Aerocapture Orbit		
Periapsis altitude	h_p	13.9 km
Apoapsis altitude	h_a	2396 km
Semi-major axis	a_1	4594.5 km
Eccentricity	e_1	0.259
Orbital Corrections and Δv Requirements		
Periapsis raise (apoapsis burn)	Δv_1	0.039 km/s
Circularisation (periapsis burn)	Δv_2	0.383 km/s
Total manoeuvre cost	Δv_{total}	0.422 km/s

The combined manoeuvre cost of $\Delta v_{\text{total}} = 0.422$ km/s demonstrates the high propulsive efficiency achieved through aerocapture compared with a conventional propulsive Mars orbit insertion. This trajectory achieves an effective balance between capture efficiency, thermal safety, and controllability, representing the most practical design point for a blunt sphere–cone vehicle performing aerocapture at Mars.

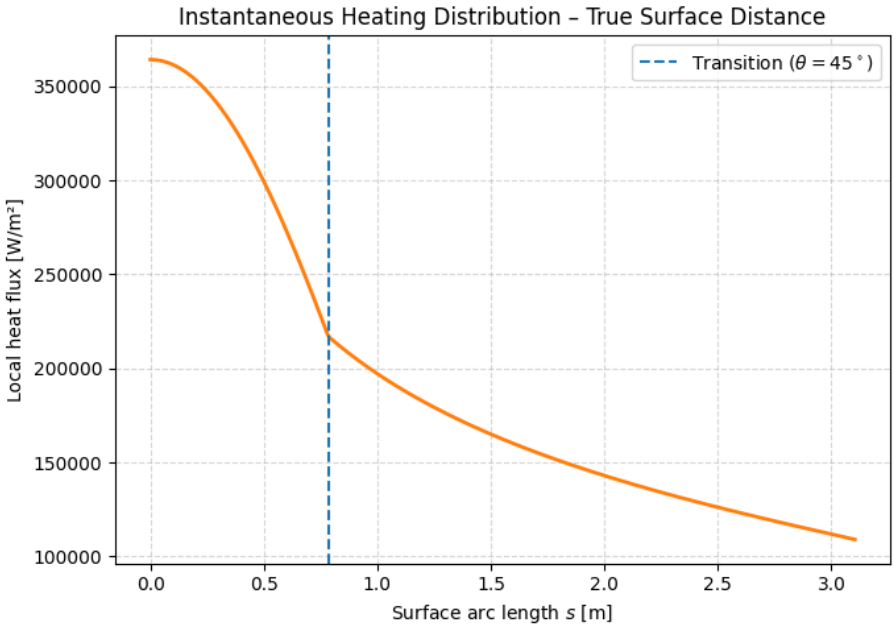

Figure 10: Local heat flux distribution across the spherical nose and conical flank for the optimal Mars entry case. The stagnation point ($x = 0$) corresponds to the maximum heating rate of 36.4 W/cm^2, decreasing along the surface with a sharp gradient near the 45° transition region.

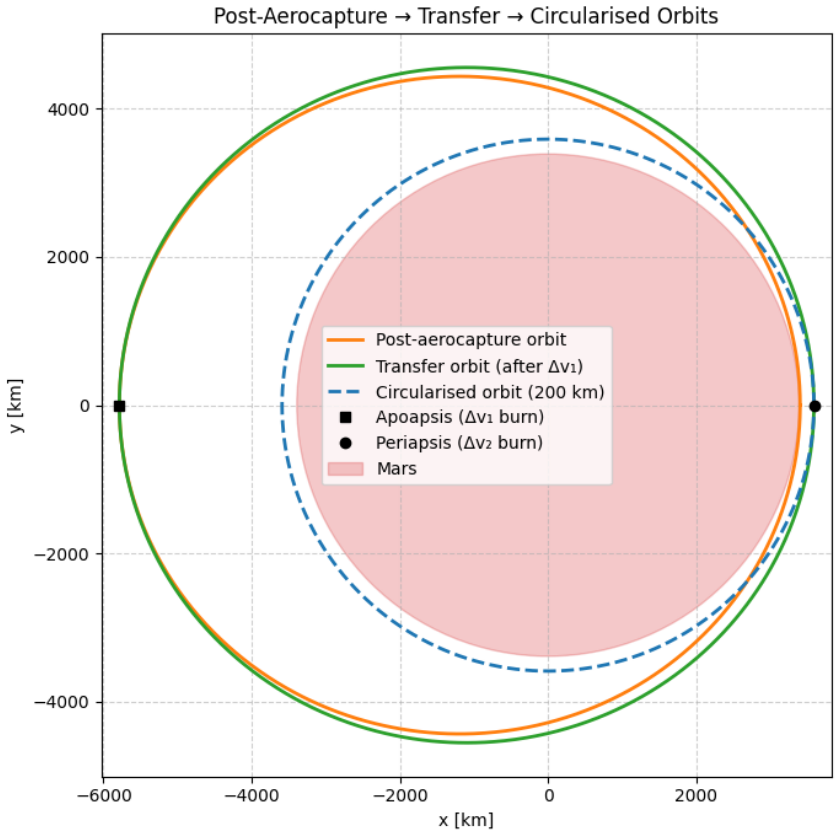

Figure 11: Post-aerocapture, transfer, and circularised orbit for the optimal trajectory. The apoapsis burn (Δv_1) raises the periapsis to 200 km altitude, followed by a periapsis circularisation burn (Δv_2) resulting in a stable circular orbit.

4 Conclusion

This study successfully developed and validated a three–degree–of–freedom (3–DOF) numerical model to simulate Mars aerocapture trajectories and evaluate both thermal and orbital performance for a blunt sphere–cone entry vehicle. The solver accurately reproduced benchmark results from the NASA aerocapture study (Matz et al., 2021), confirming the validity of the implemented equations of motion, aerodynamic models, and heating correlations.

The instantaneous heating analysis demonstrated that the implemented surface–heating routine correctly captures the transition between the stagnation–dominated spherical nose and the attached–flow conical flank, with excellent agreement against analytical predictions. The maximum heating rate of 36.4 W/cm^2, total heat load of 4.87×10^3 J/cm^2, and peak deceleration of 1.89 g indicate that the chosen geometry provides sufficient thermal and structural margins for capture in the Martian atmosphere.

The parametric aerocapture study revealed that lift–to–drag ratio and entry flight–path angle strongly influence capture efficiency and thermal loading. Low–L/D trajectories exhibited narrow and thermally demanding capture corridors, while high–L/D cases provided smoother control but diminished propulsive benefit. The intermediate configuration, $L/D = 0.4$, $\gamma_0 = -10.5°$, and $V_0 = 5.8$ km/s, was identified as the optimal solution, achieving capture with minimal heating and a total manoeuvre cost of only 0.422 km/s.

Overall, the results confirm the effectiveness of aerocapture as a highly efficient method for Mars orbital insertion, capable of reducing propulsive Δv requirements by over an order of magnitude compared to conventional chemical insertion. The developed model provides a robust computational framework for future studies involving advanced guidance schemes, variable aerodynamic configurations, and coupled thermochemical equilibrium effects to further optimise aerocapture performance.

References

[1] Richard G. Morgan. Aero4800 lecture 18: Planetary entry trajectories and ballistic entry. Based on 2024 notes from C. M. James, September 2025. URL `https://learn.uq.edu.au`.

[2] Daniel A. Matz, Ping Lu, Gavin F. Mendeck, and Ronald R. Sostaric. Application of a fully numerical guidance to mars aerocapture. Technical Report AIAA 2021-1203, NASA Johnson Space Center, Houston, TX, 2021. URL `https://arc.aiaa.org/doi/10.2514/6.2021-1203`. American Institute of Aeronautics and Astronautics, AIAA SciTech Forum, January 2021.

[3] Richard G. Morgan. Aero4800 lecture 20: Stagnation point heating. Based on 2024 notes from C. M. James, September 2025. URL `https://learn.uq.edu.au`.

[4] Richard G. Morgan. Aero4800 lecture 21: Local heat flux estimates. Based on 2024 notes from C. M. James, September 2025. URL `https://learn.uq.edu.au`.